Nonlinear oscillations, transition to chaos and escape in the Duffing system with non-classical damping

Laura Ruzziconi, [a] Grzegorz Litak, [b,a] Stefano Lenci [a,1]

[a] *Department of Architecture, Buildings and Structures, Polytechnic University of Marche, Via Brecce Bianche, I-60131 Ancona, Italy*

[b] *Department of Applied Mechanics, Lublin University of Technology, Nadbystrzycka 36, PL-20-618 Lublin, Poland*

Abstract

The nonlinear dynamics of a single-degree-of-freedom oscillator with an external excitation and complex non-viscous damping is examined. The complex nature of the damper introduces a hidden variable to the set of equations of motion. We examine nonlinear oscillations, bifurcations and the escape from the potential well in that system. The shape of the resonance curve is obtained by the multiple time scales method and it is confirmed numerically. By treating the excitation and damping effects as perturbations we found the heteroclinic orbits connecting the saddle points of the Hamiltonian and estimate the range of system parameters leading to a chaotic behaviour by means of the Melnikov method. This result is also confirmed by numerical simulations. The mechanism of escape from the potential well is analyzed by mean of behaviour charts and basins of attraction.

1 Introduction

The effects of a complex damping force depending rather on the history of the velocity than the instantaneous value have been studied numerically and analytically in last years [1–5]. Some authors proposed the damping force to be proportional to a fractional derivative of the displacement, and not as in the classical case to the order 1 derivative (i.e. the velocity) [6–9]. The memory of the system was noted to be an important factor in different areas [10]. For instance non-viscous damping with hysteresis has been investigated in the

[1] Corresponding author, *lenci@univpm.it*

context of magnetorheological fluid [11], in damping of vehicle tire [12], and in damping of plates made of composite materials [13]. The memory modelled by fractional derivatives were also applied to the problem of shock interaction of an impactor with a rigid target [14], and to study visco-elastic properties of beams, plates and cylindrical shells [10].

The dependence on the velocity history have some interesting implications: (i) it can be modeled by an appropriate integral term taking into account a natural fading memory behaviour of real systems [5], (ii) it induces an hysteretic effect [11], and (iii) it increases the effective dimension of the phase space [15], since the system memory effect can be represented by internal degrees of freedom. The damping can be expressed as the integral over some states evolution, and in the case of a single internal coordinate the kernel of the integral is usually of exponential type.

In the present paper we study the softening Duffing system with a single potential well subjected to an external harmonic excitation, and with a damping term defined by the integral convolution of an exponential kernel with the past velocity [5]. More precisely, the dynamical system is governed by the differential equation:

$$\ddot{x} + 2\zeta \int_{\tau=t_0}^{\tau=t} \frac{\mathrm{e}^{-(t-\tau)/\beta}}{\beta} \dot{x}(\tau)\mathrm{d}\tau + x + a_3 x^3 = a_0 \cos(\omega t), \tag{1}$$

where ζ is the damping coefficient, a_0 and ω are the excitation amplitude and (circular) frequency, respectively, a_3 is a *negative* number measuring the nonlinear stiffness, t_0 is the initial time and where dot means derivative with respect to time. β is the relaxation parameter and it is related to the time scale of the system memory. Similar relaxation parameters often appear in combined electro-mechanical systems [16].

Equation (1) can be rewritten in the alternative form

$$\ddot{x} + 2\zeta y + x + a_3 x^3 = a_0 \cos(\omega t), \tag{2}$$

$$\dot{y} = \frac{\dot{x} - y}{\beta}, \tag{3}$$

which better underlines the increment of the dimension of the system. Here y is the internal variable taking into account the effects of the velocity history on the actual dissipation. Note that in the limit case $\beta \to 0$, the damping force reduces to classical viscous damping [5].

The present model was originally proposed by Biot [17,18] and used in the context of dynamics of linear elastic and viscoelastic systems. Recently Eq.

(1) has been studied by Sieber *at al.* [5], who focus on the effects of the integral damping on the resonance, showing in particular the resonance peak enhancement due to β both for hardening and softening oscillators.

The present paper continues that approach by showing the dynamical features, including nonlinear oscillations, bifurcations and transition to chaos, in the case of the strong nonlinearity in the softening Duffing equation with a single potential well.

The paper is organized as follows. After the present introduction, we will study (Sec. 2) the system nonlinear resonance by analytical and numerical methods. Sec. 3 is devoted to the Melnikov analysis and to the appearance of transient chaotic solution. On the other hand, Sec. 4 concerns with the escape phenomenon. Finally, in Sec. 5, the paper ends with the summary and final conclusions.

2 Nonlinear resonance

In this section we study the nonlinear resonance of the considered system, paying attention of the resonant and to the non-resonant attractors, and to their bifurcations.

2.1 Approximate analytical solution

We start by using the multiple scale method (MSM) [19,20], which provides an analytical approximate solution and thus permits to detect the effects of the main parameters, and in particular of β, on the system response.

To apply the MSM we introduce the small parameter ε and rewrite Eq. (2) in the form

$$\ddot{x} + 2\varepsilon\zeta' y + x + \varepsilon a_3' x^3 = \varepsilon a_0' \cos(\omega t), \tag{4}$$

where $\zeta = \varepsilon\zeta'$, $a_3 = \varepsilon a_3'$, and $a_0 = \varepsilon a_0'$, while Eq. (3) is left unchanged.

As usual with the MSM [19], we define the fast and slow times $T_0 = t$, $T_1 = \varepsilon t$, $T_2 = \varepsilon^2 t$, ... , and we assume that (we report only the expressions for x; the expressions for y are identical)

$$x(t) = x(t, \varepsilon t, \varepsilon^2 t, ...) = x(T_0, T_1, T_2, ...). \tag{5}$$

The time derivatives are then

$$\begin{aligned}\dot{x} &= D_0 x + \varepsilon D_1 x + ..., \\ \ddot{x} &= D_0^2 x + 2\varepsilon D_1 D_0 x + ...\end{aligned} \tag{6}$$

where

$$D_i x = \frac{\partial}{\partial T_i} x(T_0, T_1, T_2, ...). \tag{7}$$

The solution is sought in the ε-series form

$$x(T_0, T_1, T_2, ...) = x_0(T_0, T_1, T_2, ...) + \varepsilon x_1(T_0, T_1, T_2, ...) + ... \tag{8}$$

After substituting x given by Eq. (8) and its derivatives given by Eq. (6) - and identical expressions for y - in Eq. (3) and Eq. (4), and after collecting the coefficients of increasing power n of ε^n, we obtain a sequence of ordinary differential equations for x_i and y_i.

By setting equal to zero the coefficient of ε^0 in Eq. (4) we get the first equation

$$D_0^2 x_0 + x_0 = 0, \tag{9}$$

which has the solution

$$x_0 = A(T_1, T_2, ...)\mathrm{e}^{\mathrm{i}T_0} + cc, \tag{10}$$

where $A(T_1, T_2, ...)$ is the slow-times dependent amplitude and the abbreviation cc denotes complex conjugates. In the following only the slow time T_1 will play a role, so we assume $A(T_1)$.

The approximate solution (10) is used in the computation of the lowest approximation of y. In fact, by setting equal to zero the coefficient of ε^0 in Eq. (3) we get the equation

$$\dot{y_0} = \frac{\dot{x_0} - y_0}{\beta}, \tag{11}$$

whose steady state solution is

$$y_0 = \frac{\mathrm{i}A\mathrm{e}^{\mathrm{i}T_0}}{\mathrm{i}\beta + 1} + cc. \tag{12}$$

To have the frequency in the range of resonance we assume the excitation frequency $\omega = 1 + \varepsilon\sigma$, where σ is the detuning parameter (note that the undamped natural frequency is $\omega_{\mathrm{res}} = 1$). The forcing harmonic factor then becomes

$$\cos(\omega t) = \cos(t + \varepsilon t\sigma) = \cos(T_0 + \sigma T_1) = \frac{1}{2}\mathrm{e}^{\mathrm{i}(T_0+\sigma T_1)} + cc. \tag{13}$$

The ε^1-coefficient of Eq. (4) yields

$$D_0^2 x_1 + x_1 = -2D_0 D_1 x_0 - 2\zeta y_0 - a_3' x_0^3 + a_0' \left(\frac{1}{2}\mathrm{e}^{\mathrm{i}(T_0+\sigma T_1)} + cc\right). \tag{14}$$

Terms multiplying $\mathrm{e}^{\mathrm{i}T_0}$ on the right hand side of (14) provide secular terms. They give a non-stationary solution and therefore they are physically not acceptable. To eliminate these terms we must set equal to zero the coefficient of $\mathrm{e}^{\mathrm{i}T_0}$. This gives

$$2\mathrm{i}\frac{\mathrm{d}A}{\mathrm{d}T_1} + 2\zeta\frac{\mathrm{i}A}{\mathrm{i}\beta + 1} + 3A^2\overline{A}a_3' - \frac{a_0'\mathrm{e}^{\mathrm{i}\sigma T_1}}{2} = 0, \tag{15}$$

where $\overline{A}$ is a complex conjugate to A. By expressing the complex amplitude A in the polar form

$$A = b\mathrm{e}^{\mathrm{i}\Theta}, \tag{16}$$

where b and Θ are real, we can split the equation into the real and imaginary parts:

$$\begin{aligned} 2\frac{\mathrm{d}b}{\mathrm{d}T_1} + \frac{2\zeta' b}{1+\beta^2} - \frac{a_0'}{2}\sin\gamma = 0, \\ 2b\frac{\mathrm{d}\gamma}{\mathrm{d}T_1} + 3b^3 a_3' - 2\sigma b + \frac{2\beta\zeta' b}{1+\beta^2} - \frac{a_0'}{2}\cos\gamma = 0. \end{aligned} \tag{17}$$

Note that in the above expression $\gamma = \sigma T_1 - \Theta$. For steady state solutions

$$\frac{\mathrm{d}b}{\mathrm{d}T_1} = 0 \qquad \text{and} \qquad \frac{\mathrm{d}\gamma}{\mathrm{d}T_1} = 0, \tag{18}$$

which provide

$$\frac{2\zeta' b}{1+\beta^2} = \frac{a'_0}{2}\sin\gamma,$$
$$3b^3 a'_3 - 2\sigma b + \frac{2\beta\zeta' b}{1+\beta^2} = \frac{a'_0}{2}\cos\gamma. \tag{19}$$

By eliminating γ from Eq. (19) we get the nonlinear expression linking the amplitude b and detuning parameter σ:

$$\frac{(a'_0)^2}{4} = \left(\frac{2\zeta' b}{1+\beta^2}\right)^2 + \left(3b^3 a'_3 - 2\sigma b + \frac{2\beta\zeta' b}{1+\beta^2}\right)^2. \tag{20}$$

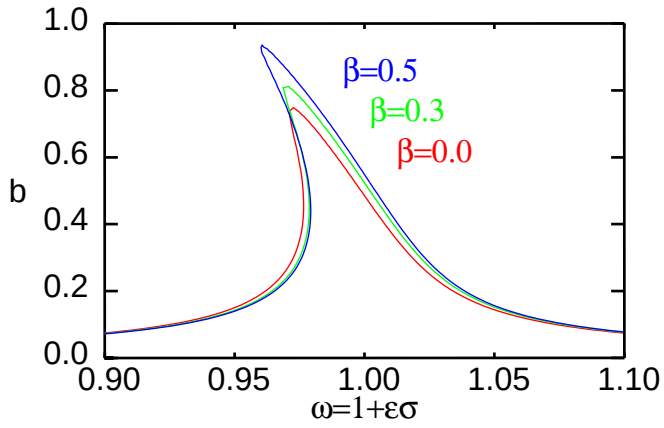

Fig. 1. (color online) Approximate resonance curves obtained by the method of multiple scales for three values of β ($\beta = 0.0$; 0.3; 0.5) and $\varepsilon = 0.1$, $a'_0 = 0.3$, $a'_3 = -0.5$ and $\zeta' = 0.1$.

The solution of the above algebraic equation is plotted in Fig. 1. Note that nonzero β lowers damping. This fact can be inferred by noting that for an harmonic oscillation $x(t) = \alpha\cos(\omega t)$ we have $y(t) = \frac{\alpha\omega}{\sqrt{1+\beta^2\omega^2}}\cos(\omega t + \varphi)$, so that

$$\frac{|y|}{|\dot{x}|} = \frac{1}{\sqrt{1+\beta^2\omega^2}}, \tag{21}$$

which shows that $|y| < |\dot{x}|$, namely, the integral damping is smaller that the classical damping for $\beta > 0$ (see Eq. (2)).

Note also that the resonance curves bend toward low frequencies (Fig. 1) because of the negative value of the nonlinear term a_3' (softening behaviour).

The locus of the maximum points of the curves $b(\sigma)$ is obtained by differentiating Eq. (20) with respect to σ and by setting $b'(\sigma) = 0$. This gives the so-called backbone curve

$$\sigma = \frac{3}{2} b_{\max}^2 a_3' + \frac{\beta \zeta'}{1 + \beta^2}, \tag{22}$$

which further underlines the damping effect due to β and the fact that the sign of a_3' determines the softening vs hardening behaviour of the system.

2.2 Numerical simulations

More detailed bifurcation studies of Eq. (1) have been performed by numerical simulations, following the same lines of [21]. Using attractors-basin phase portraits, bifurcation diagrams, path following and time histories allow us both to investigate in detail the main features and to verify the concurrence of results coming form different tools. These results are mainly obtained by the aid of the software packages AUTO [22] and Dynamics [23], and are checked with a lot of episodic investigations with self-developed codes.

In this section we focus on numerical bifurcation diagrams, which are aimed at checking the analytical predictions of Sec. 2.1 and at extending the results by detecting, e.g., pitchfork bifurcations and crises. The other dynamical features investigated numerically will be addressed in the next sections.

For the fairly small fixed value $a_0 = 0.025$ of the excitation amplitude the path following of the maximum displacement has the typical shape of a nonlinear oscillator with softening behaviour, as shown in Fig. 2a (see also Fig. 1b in [5]). It has both a resonant and a non-resonant branch and it shows the characteristic bending of the resonance peak towards lower frequencies. This is in perfect agreement with the analytical results of Fig. 1.

For increasing values of a_0 (Fig. 2b) the non-resonant branch A1 does not change qualitatively its behaviour, and disappears at $\omega \cong 0.8$ by a saddle-node bifurcation. On the resonant branch A2, on the other hand, a new event appears. In fact, the resonant oscillation loses stability by a pitchfork (or symmetry breaking) bifurcation occurring before (for decreasing values of ω)

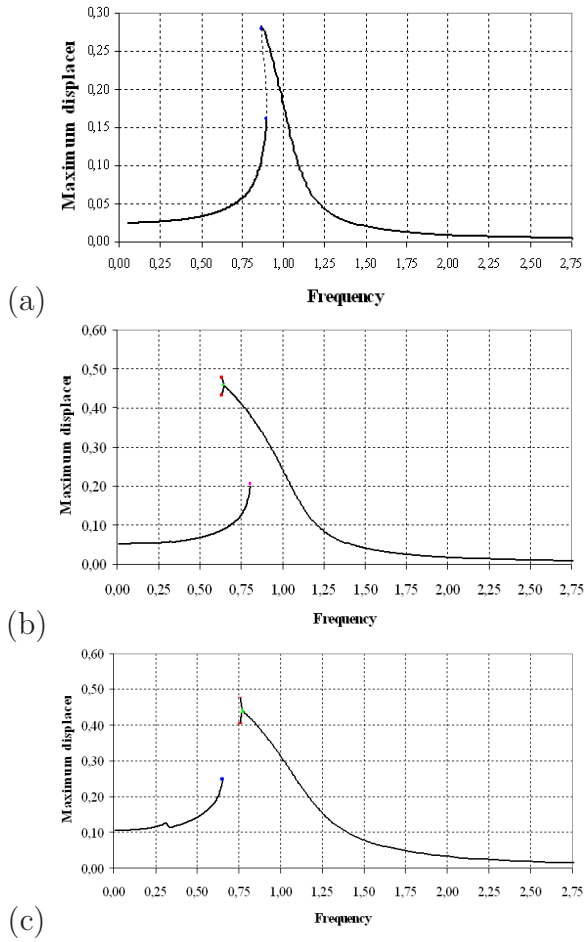

Fig. 2. Resonance curves obtained numerically for different excitation amplitudes. (a) $a_0 = 0.025$, (b) $a_0 = 0.05$ and (c) $a_0 = 0.1$. Other system parameters are $a_3 = -4.0$, $\zeta = 0.05$, and $\beta = 0.05$. The lower-left non-resonant branch is denoted A1, while the upper-right resonant branch is named A2.

the upper saddle-node. Then, each of the two new attractors (denoted A3 and A4) develops a cascade of period-doubling bifurcations leading to a chaotic motion which, after some interior crises, finally disappear by a boundary crisis. However, both the cascade and the chaotic region occur in a very narrow range of the system parameters, and so they are not visible in Fig. 2b.

It is worth to note that the resonant and the non-resonant branches still coexist for a quite wide range of ω. However, increasing a_0, this range becomes smaller and smaller, and finally disappears. In fact, Fig. 2c shows that for $a_0 = 0.1$ a short gap of ω appears with no bounded solutions. This is the escape area where the solution diverges for any initial conditions.

We can better observe this phenomenon Fig. 3, which is obtained by building several bifurcation diagrams similar to those of Fig. 2 and by reporting the main bifurcational events (Fig. 3a) and the escape region (Fig. 3b).

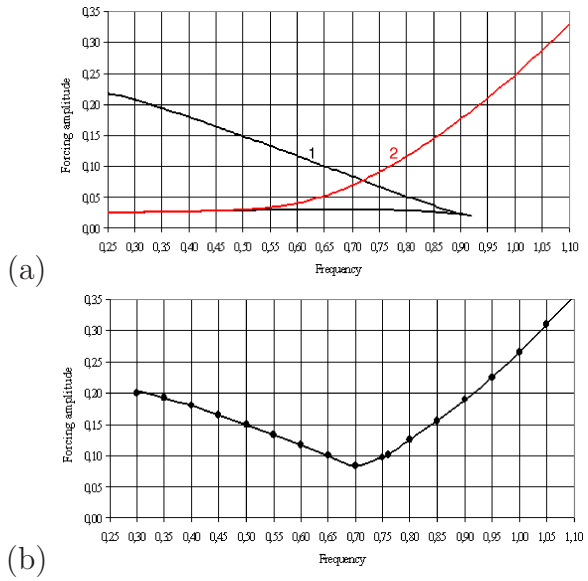

Fig. 3. (Color online) (a) Frequency-amplitude behaviour chart. Saddle-node bifurcation (black line, 1) and pitchfork bifurcation (red line, 2) are reported. (b) Escape curve (the escape area is above the curve). $\zeta = 0.05$; $a_3 = -4$; $\beta = 0.05$.

The escape region has the classical V-shape, with the vertex in the codimension 2 point where the pitchfork and the upper saddle-node coincide [24]. Above this point the non-resonant attractor disappears before (for increasing ω) the appearance of the resonant branch, thus producing the escape, which will be better investigated in Sec. 4.

3 Melnikov analysis and transient chaos appearance

The escape phenomenon is related to the erosion of the basins of attraction belonging to the unique potential well by means of the out-of-well attractor. Thus, it is worth to preliminary study the heteroclinic bifurcation of the hilltop saddles, which is the mechanism responsible for the triggering of the erosion, successively leading to escape. The heteroclinic bifurcation threshold can be analytically detected by the Melnikov method [25–27].

In the present section we apply the Melnikov method to the system (1). The novelty of this application in the context of the Melnikov approach is the extension of the original phase space dimension from 2 to 3 due to the hidden variable y associated the memory effect (Eqs. (2) and (3)).

To perform the Melnikov analysis we introduce the small parameter ε into the differential equation (2) and rewrite the governing system as the set of the first order differential equations

$$
\begin{aligned}
\dot{x} &= v, \\
\dot{v} &= -x - a_3 x^3 + \varepsilon(-2\zeta' y + a_0' \cos(\omega t)), \\
\dot{y} &= \frac{v - y}{\beta}.
\end{aligned}
\tag{23}
$$

Note that we rescale the parameters ζ and a_0 as in Sec. 2.1, while a_3 remains unchanged.

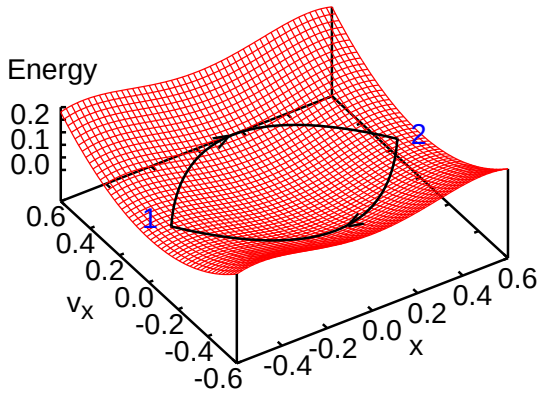

Fig. 4. (Color online) The energy $H(x, v)$ for $a_3 = -4$ in the unperturbed ($\varepsilon = 0$) system. The full black oriented lines denote the heteroclinic orbits connecting two saddle points '1' and '2'.

The unperturbed Hamiltonian equations associated to Eq. (23) are

$$
\begin{aligned}
\dot{x} &= v, \\
\dot{v} &= -x - a_3 x^3,
\end{aligned}
\tag{24}
$$

while the Hamiltonian and the corresponding potential are

$$
H(x, v) = \frac{v^2}{2} + V(x), \tag{25}
$$

$$
V(x) = \frac{x^2}{2} + a_3 \frac{x^4}{4}, \tag{26}
$$

respectively. Note that $a_3 < 0$ guarantees the presence of two symmetric hilltop saddles at $x = \pm\sqrt{-1/a_3}$ (Fig. 4). They are connected by the two symmetric heteroclinic orbits

$$x^* = \pm\sqrt{\frac{-1}{a_3}}\ \tanh\left(\frac{t}{\sqrt{2}}\right), \tag{27}$$

$$v^* = \pm\sqrt{\frac{-1}{2a_3}}\cosh^{-2}\left(\frac{t}{\sqrt{2}}\right). \tag{28}$$

The expression of the component y^* of the heteroclinic orbit can be obtained by solving (3), which becomes

$$\dot{y}^* = \pm\frac{1}{\beta}\sqrt{\frac{-1}{2a_3}}\cosh^{-2}\left(\frac{t}{\sqrt{2}}\right) - \frac{y^*}{\beta} \tag{29}$$

and has solution (use is made of the condition $\lim_{t\to-\infty} y^*(t) = 0$)

$$y^* = \pm\frac{1}{\beta}\sqrt{\frac{-1}{2a_3}}\mathrm{e}^{-t/\beta}\int_{-\infty}^{t}\frac{\mathrm{e}^{\tau/\beta}}{\cosh^2(\tau/\sqrt{2})}\mathrm{d}\tau. \tag{30}$$

The Melnikov integral $M(t_0)$ can be written as [26]

$$M(t_0) = \int_{-\infty}^{\infty} v^*(t)[-2\zeta' y^*(t) + a_0'\cos(\omega(t-t_0))]\mathrm{d}t. \tag{31}$$

The above integral splits in the two parts (use is made of the time symmetry of v^*)

$$M(t_0) = -2\zeta' M_1 + a_0'\cos(\omega t_0)M_2, \tag{32}$$

where

$$M_1 = \int_{-\infty}^{\infty} v^*(t)y^*(t)\mathrm{d}t, \tag{33}$$

$$M_2 = \int_{-\infty}^{\infty} v^*(t)\cos(\omega t)\mathrm{d}t. \tag{34}$$

The second integral M_2 can be estimated by the theory of residue,

$$M_2 = \frac{\sqrt{2}\pi\omega}{\sqrt{-a_3}} \frac{1}{\sinh(\pi\omega/\sqrt{2})}, \tag{35}$$

while the first integral M_1 must be integrated numerically using Eq. (28) and Eq. (30).

According to the Melnikov theory we have heteroclinic intersections if and only if there exists a t_0 such that

$$M(t_0) = 0, \qquad \frac{\partial M(t_0)}{\partial t_0} \neq 0. \tag{36}$$

From (32) this occurs, simultaneously in the upper and lower heteroclinic orbit, when

$$\frac{a_0}{2\zeta} = \frac{a_0'}{2\zeta'} \geq \left|\frac{M_1}{M_2}\right| = \left(\frac{a_0}{2\zeta}\right)_{cr}. \tag{37}$$

The critical threshold is reported in Fig. 5 as a function of ω (Fig. 5a) and as a function of β (Fig. 5b). It is worth to remark that above the critical curve we have fractal basin boundaries. Moreover, through this fractalization the basin of attraction of the escape solution starts to enter the potential well and to erode the in-well basins.

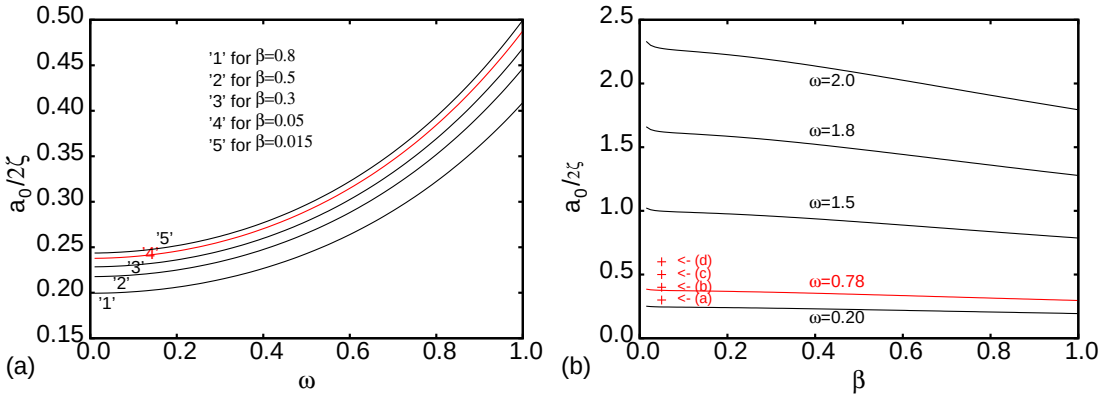

Fig. 5. (Color online) The critical threshold $(a_0/2\zeta)_{cr}$ versus (a) frequency and (b) the coefficient β. The area below the curves indicate the regular solutions while above them the corresponding solutions have sensitivity to initial conditions, chaotic transient and fractal basin boundaries. The pluses in (b) correspond to the points where the basins of attraction of the next Figs. 6a-d are built. $a_3 = -4$.

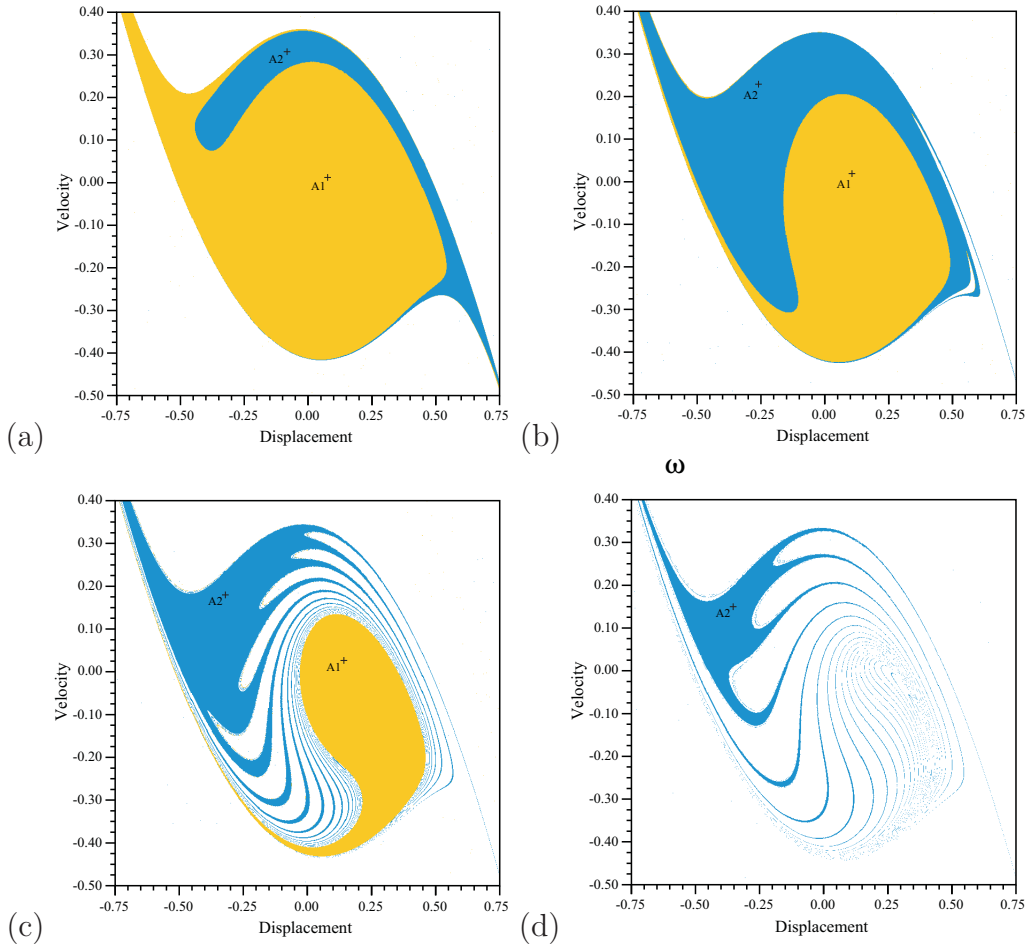

Fig. 6. (Color online) 2D sections at $y = 0$ of the 3D basins of attraction for $\zeta = 0.05$, $a_3 = -4$, $\beta = 0.05$, $\omega = 0.78$ and (a) $a_0 = 0.03$, (b) $a_0 = 0.04$, (c) $a_0 = 0.05$, and (d) $a_0 = 0.06$. Yellow, A1: non-resonant attractor; blue, A2: resonant attractor; white: out-of-well (escape) attractor.

To confirm the analytical predictions we consider 2D sections at $y = 0$ of the 3D attractor-basins phase portraits. For the given excitation frequency $\omega = 0.78$ and for increasing excitation amplitude a_0 they are reported in Fig. 6.

For low values of a_0 (Fig. 6a) we have the resonant A2, previously appeared by a saddle-node bifurcation (see Figs. 2a and 3), and the non-resonant A1 attractors which coexist within the potential well. They have a smooth reciprocal basin boundary (color to color); furthermore, since we are below the heteroclinic bifurcation threshold, also the white to color boundary with the out-of-well attractor (white basin) is smooth.

Although coexisting and although being both period-1 oscillations, resonant and non-resonant attractors have very different maximum displacement and velocity; for example, the time history of the displacement (Fig. 7a) shows that the resonant attractor has an amplitude which is about 4 times that of

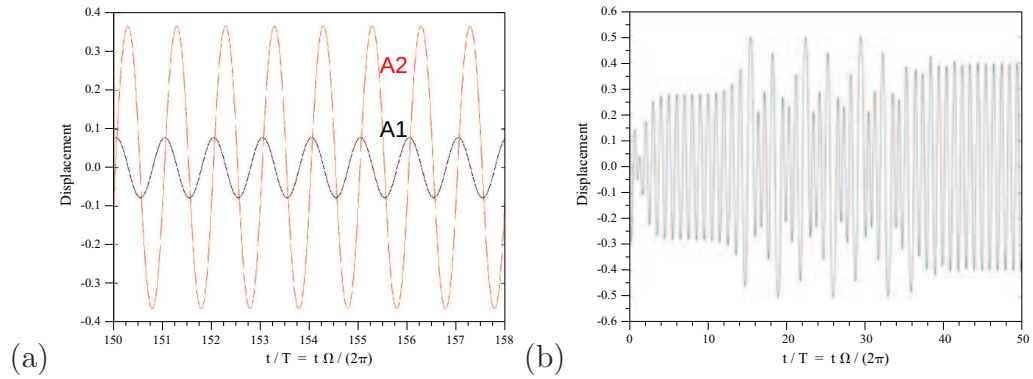

Fig. 7. (Color online) Time histories for (a) resonant (A1) and non-resonant (A2) periodic oscillations ($a_0 = 0.03$) and (b) a chaotic transient ($a_0 = 0.05$). $\omega = 0.78$, $\zeta = 0.05$, $a_3 = -4$ and $\beta = 0.05$.

the non-resonant one.

In Fig. 6a the resonant attractor was just born, and this is why it has a small basin of attraction. For increasing forcing amplitude a_0, the basin of A2 grows against that of A1 (Fig. 6b). Furthermore, as soon as we cross the heteroclinic bifurcation threshold (an event which occurs in between Figs. 6a and 6b, see Fig. 5b), fractal basins boundaries are observed (Fig. 6b).

The fractality first appears on the border between A2 and the out-of-well attractor (Fig. 6b), but for increasing a_0 it spreads (Figs. 6c and 6d), then affecting those parts of the basin which originally were deep inside the basin of A2. Thus, we can conclude that the main consequence of the increment of a_0 is a reduction of the dynamical integrity [28,29] of A2 and of the robustness of A1 (in fact, the basin of A1 is not fractal but only reduces its dimension). It is worth to note that the present numerical results confirm the Melnikov prediction. All the analyzed cases plotted in Figs. 6a-d have been denoted in Fig. 5b by pluses. The case (a) is below the Melnikov critical curve (for $\omega = 0.78$) while the cases (b)-(d) are above. One can see that the fractalization of the boundary basins visible in Figs. 6b-d coincides with the global transition indicated by the Melnikov criterion (Eq. 37).

In the fractal areas small changes in the initial conditions can lead to different attractors. As a consequence of this sensitivity to initial conditions, we do not know exactly in advance the final response of our system. The motion becomes unpredictable, even if the system is completely deterministic.

Depending on the fractality 'magnitude' of the basin, the system response can exhibit relatively short, fairly long transient, or fully developed chaotic behaviours. A chaotic transient is a long series of erratic oscillations occurring before the system settles onto one or the other attractor. An example of is reported in Fig. 7b, where we see that the chaotic transient lasts for about 40 excitation periods before approaching the attractor A2. Note that usually

for regular motion 10 periods are enough to reach the attractor. Thus, if the chaotic transient is long enough, it has the same practical consequences of a chaotic attractor. We can conclude that this fractal area implies unpredictability both in the final response and in the transient behaviour of the analyzed system, and thus it is likely unwanted from a practical point of view.

A further increment of the excitation amplitude causes the disappearance of the non-resonant attractor A1 by an inverse saddle-node bifurcation (Figs. 2a and 3). Figure 6d shows how the resonant attractor A2 remains the unique attractor within the potential well. At this level, the fractality spread all around the potential well. Only around A2 there is compact part of the basin representing the (residual) robustness of the attractor with respect to accidental changes in initial conditions, i.e. the (residual) dynamical integrity.

In the previous case the main role is played by the two saddle-node bifurcations where A1 and A2 are born/disappear, and by the heteroclinic bifurcation triggering the fractal erosion of the dynamical integrity. However, we have seen in Figs. 2b and 2c that also the period-doubling bifurcation plays an important role for different values of the parameters. To highlights its effects, we have reported in Fig. 8 three different basins of attraction for $\omega = 1.0$. Note that only the resonant attractor A2 is present.

At $a_0 = 0.2$ (Fig. 8a) the fractalization of the basin boundaries is already advanced, since we are well above the heteroclinic bifurcation threshold. The basin of A2 has both a small compact part, which implies a reduced dynamical integrity, and a small magnitude (including fractal parts), meaning that it is difficult to catch the attractor by random initial conditions. It follows that the escape is the most probable final outcome.

In Fig. 8a we are still below the pitchfork bifurcation. At $a_0 = 0.25$ (Fig. 8a), on the other hand, the pitchfork bifurcation was occurred, and A2 is substituted by the two new period-1 attractors A3 and A4, which share the former basin of A2 (which further reduced since a_0 increased). The basins are regular; the boundary is constituted by the stable manifold of the period-1 oscillation which loss stability (and becomes a saddle) at the pitchfork bifurcation.

At $a_0 = 0.2663$ (Fig. 8c) A3 and A4 become chaotic attractors. Both are confined in a very narrow region of the phase space, so that the chaoticity is not very pronounced. However, the principal feature is that the basins of attraction are completely fractal and shrunk, while the white area is wider and wider with respect to the other cases.

It is worth to underline that, even if the $a_0 - \omega$ diagram shows the presence of attractors up to the escape curve, the attractor-basins phase portrait reveals that these attractors have so small basins and integrity that, from a practical point of view, they can be neglected.

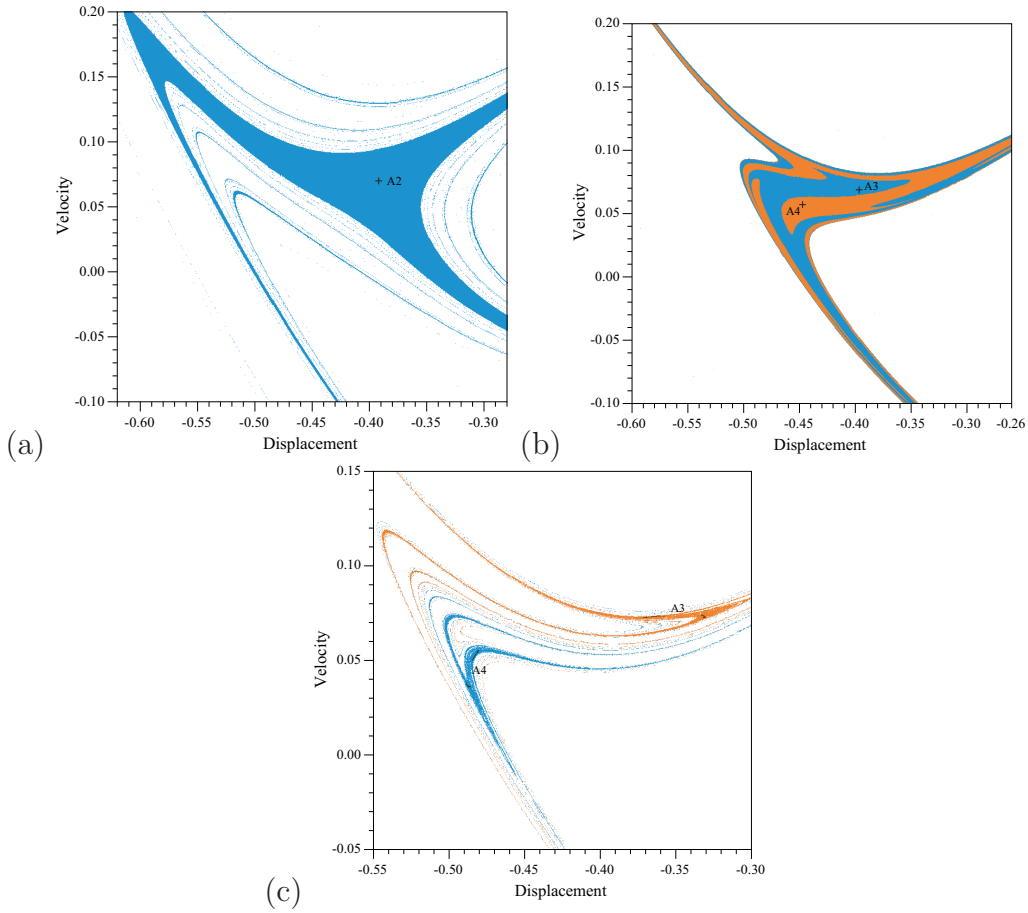

Fig. 8. (Color online) 2D sections at $y = 0$ of the 3D basins of attraction for (a) $a_0 = 0.2$, (b) $a_0 = 0.25$ and (c) $a_0 = 0.2663$. $\omega = 1.0$, $\zeta = 0.05$, $a_3 = -4$ and $\beta = 0.05$.

We can conclude that, even if the two attractors disappear by boundary crisis, the transition to the escape is not so sudden, but it is progressive and clearly forewarned both by the increment in the initial conditions leading to the escape area, and by the simultaneous complete destruction of the dynamical integrity of the attractors. In this particular case, this transition is also associated with an extensive fractality of the basin boundaries, and with a sequence of bifurcations of the attractor up to its final disappearing.

4 Escape from the potential well

In the previous Fig. 3b we anticipated the numerically obtained escape curve. In Fig. 9 we compare it with the Melnikov threshold for heteroclinic bifurcation. The latter is the starting point of the dynamical integrity erosion proceeding for increasing values of a_0 (see Fig. 6), while the former is the ending point of the erosion.

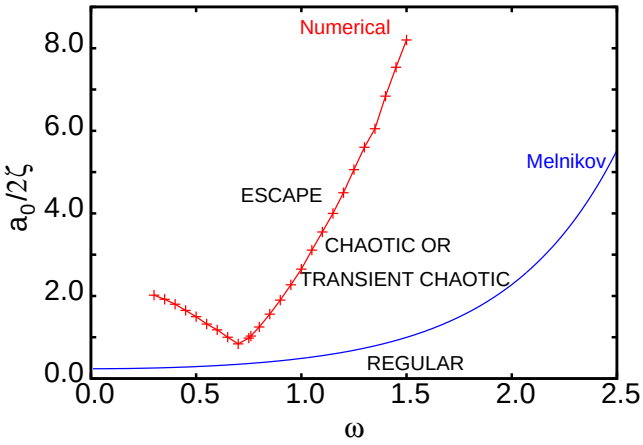

Fig. 9. (Color online) Escape vs heteroclinic bifurcations (Melnikov) thresholds. $\zeta = 0.05$, $a_3 = -4$ and $\beta = 0.05$.

Although being the initial and the final point of erosion, these two thresholds are due to completely different phenomena (heteroclinic bifurcation of the hilltop saddle, the first, disappearance of the last in-well attractor, the second) and thus they are some uncorrelated. This is confirmed by the fact that they have different shapes. In fact, for example, while the Melnikov curve is not influenced by the resonance, the escape curve is influenced, since resonance entails large oscillations which facilitate the escape from the potential well. This is confirmed by Fig. 9, which shows that escape curve has a minimum at about $\omega = 0.70$, which is close to the resonant frequency $\omega = 1.0$. The Melnikov curve, on the other hand, has not a minimum.

Roughly speaking, we can say that the Melnikov curve is influenced by what happens at the top of the potential well, while escape curve is also susceptible to what happen at the bottom of the well.

We now analyze what the minimum in the escape curve means in terms of dynamical integrity. We compare four different cases (Figs. 10 and 11) at $a_0 = 0.1$, i.e. slightly above the minimum of the escape curve.

For $\omega = 0.225$, i.e. on the left of the vertex of the escape curve of Fig. 9, A1 is the unique attractor of the system. Its basin, plotted in Fig. 10a, is wide and with smooth boundaries.

As soon as ω increases and gets closer to the resonant frequency, the basin strongly reduces in size, as shown in Fig. 10b, which corresponds to $\omega = 0.65$ and it is very close to the escape curve. Even if we apply the same forcing amplitude, a shift in the excitation frequency towards the resonance is able to produce the escape of almost all initial conditions. The fall of the dynamical integrity of the attractor clearly forewarns the transition to the

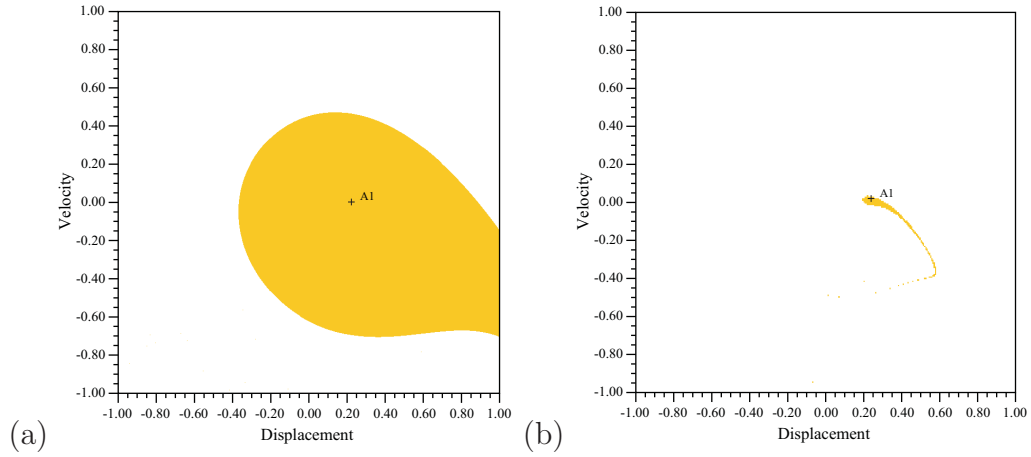

Fig. 10. (Color online) 2D sections at $y = 0$ of the 3D basins of attraction for $a_0 = 0.1$, $\zeta = 0.05$, $a_3 = -4$ and $\beta = 0.05$. (a) $\omega = 0.225$; (b) $\omega = 0.65$.

complete escape from the potential well. Another small increment of ω, in fact, destroy the A1 attractor, and in fact in the range $0.66 < \omega < 0.75$ we have that no in-well attractors exist: we are in the escape region of Fig. 9.

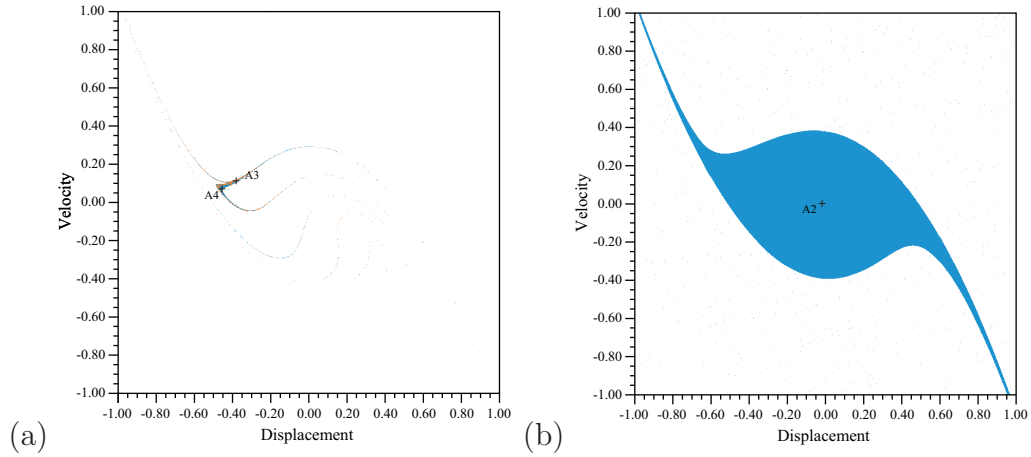

Fig. 11. (Color online) 2D sections at $y = 0$ of the 3D basins of attraction for $a_0 = 0.1$, $\zeta = 0.05$, $a_3 = -4$ and $\beta = 0.05$. (a) $\omega = 0.76$; (b) $\omega = 2.50$.

The in-well attractors reappears at $\omega = 0.76$ (Fig. 11a), which is just above the escape region. At the beginning, it has a residual dynamical integrity (Fig. 11a), which however increases as we move away from the escape region (Fig. 11b). Again, as before, we see that the transition to escape (now by *decreasing* values of ω) is forewarned by the destruction of the dynamical integrity. In this case, it is also associated both with fractal basin boundaries and with a pitchfork bifurcation of the resonant branch where the attractors A3 and A4 were born.

5 Summary and Conclusions

In this paper we investigated local and global bifurcations of a softening Duffing oscillator with a non-classical damping term taking into account the past history of the velocity. This memory term is of integral type with an exponential kernel, and thus it is of fading type with a given time length β of 'relaxation.' This is the main parameter.

We initially investigated the nonlinear oscillations around the resonant frequency, and found that, as expected, the memory terms contributes to the overall damping of the system, although it is smaller than in the classical case, a fact that confirms the findings of [5]. Detailed calculations have been done by means of the multiple scale method.

We then studied the global behaviour of the system, by paying attention to the problem of the dynamical integrity.

The heteroclinic bifurcation of the hilltop saddles have been analytically detected by a 3D version of the Melnikov method. The analytic results have been compared with numerical simulations, which confirm how above the Melnikov threshold the erosion of the basins of the in-well attractors develops up to the final escape, i.e. up to the final disappearance of any in-well attractor.

A detailed analysis of the escape phenomenon is carried out by the combined used of bifurcation diagrams and of basins of attraction.

We have shown how the fractal basins of attraction can lead to unpredictability of the system response and to a chaotic transient, which my be dangerous in applications. However, even with fractal basins, there is a compact part around the attractor, which represents the robust (or the integer) part of the basin. From a design point of view, this is the unique relevant part of the basin. If it is large enough, the design is safe against unexpected changes in initial conditions, otherwise the system loses 'practical' stability. We refer to [28,29] for more details on this important issue. Here we limit to remark the importance of the global analysis, performed by the combined use of path following and attractor-basins phase portraits, to have reliable results in terms of dynamical integrity.

In this paper a relatively small value of β is used. Larger values of β require three dimensional basins of attraction, which are more difficult to be obtained and more expensive in terms of CPU time. This issue is left for future works.

Acknowledgements

This paper has been partially supported by the 7th Framework Programme, contract No. FP-7 245479. GL would like to thank prof. S. Lenci for hospitality in Ancona and dr. M. Siewa Siewa for discussions.

References

[1] Padovan J, Sawicki JT. Nonlinear vibration of fractionally damped systems. Nonlin Dyn 1998;16:321–36.

[2] Seredynska M, Hanyga A. Nonlinear differential equations with fractional damping with application to the 1dof and 2dof pendulum. Acta Mech 2005;176:169–83.

[3] Gao X, Yu J. Chaos in the fractional order periodically forced complex Duffing's systems. Chaos Solit Fractals 2005;24:1097–104.

[4] Sheu LJ, Chen HK, Tam LM. Chaotic dynamics of the fractionally damped Duffing equations. Chaos Solit Fractals 2007;32:1459–68.

[5] Sieber J, Wagg DJ, Adhikari S. On the interaction of exponential non-viscous damping with symmetric nonlinearities. J Sound Vibr 2008;314:1–11.

[6] Terenzi G. Dynamics of SDOF systems with nonlinear viscous damping. J Eng Mech 1999;125:956–63.

[7] Trueba JL, Rams J, Sanjuan MAF. Analytical estimates of the effect of nonlinear damping in some nonlinear oscillators. Int J Bifur Chaos 2000;10:2257–67.

[8] Mikens RE, Oyedeji KO, Rucker SA. Analysis of the simple harmonic oscillator with fractional dampling. J Sound Vibr 2003;268:839–42.

[9] Litak G, Borowiec M, Syta A. Vibration of generalized double well oscillators. Zeit Angew Math Mech 2007;87:590–602.

[10] Rossikhin YA, Shitikova MV. Application of fractional calculus for dynamic problems of solid mechanics: Novel trends and recent results. App Mech Rev 2010;63:010801.

[11] Rodriguez A, Iwata N, Ikhouane F, Rodellar J. Model identification of a large-scale magnetorheological fluid damper. Smart Mat Str 2009;18:015010.

[12] Kao BG. Three-dimensional dynamic tire model for vehicle dynamic simulations. Tire Scien Tech 2000;28:72–95.

[13] Kuo P-Y, Wang S-Y, Chen J-H, Hsueh H-C, Tsai M-J. Effects of material compositions on the mechanical properties of woodplastic composites manufactured by injection molding. Mater Design 2009;30:3489–96.

[14] Atanackovic TM, Spasic DT. On viscoelastic compliant contact–impact models. ASME J. Appl. Mech. 2004;71:134–38.

[15] Lin G, Feeny BF, Das T. Fractional derivative reconstruction of forced oscillators. Nonlin Dyn 2009;55:239–50.

[16] Erturk A, Hoffmann J, Inman DJ. A piezomagnetoelastic structure for broadband vibration energy harvesting. App Phys Lett 2009;94:254102.

[17] Biot MA. Variational principles in irreversible thermodynamics with application to viscoelasticity. Phys Rev 1995;97:1463–9.

[18] Biot MA. Linear thermodynamics and the mechanics of solids. Proc of the Third U. S. National Congress on Applied Mechanics 1958, p. 1–18.

[19] Nayfeh AH. Perturbation Methods. New York:Wiley; 1974.

[20] Litak G, Spuz–Szpos G, Szabelski K, Warmiński J, Vibration of externally forced Froude pendulum. Int J Bif Chaos 1999;9:561–70.

[21] Lenci S, Ruzziconi L. Nonlinear phenomena in the single-mode dynamics of a cable-supported beam. Int J Bif Chaos 2009;10:923–45.

[22] Doedel EJ, Champneys AR, Fairgrieve TF, Kuznetsov YA, Sandstede B, Wang X. AUTO97, Continuation and bifurcation software for ordinary differential equations. Concordia University, 1998.

[23] Nusse HE, Yorke JA. Dynamics. Numerical Explorations. New York: Springer-Verlag; 1998.

[24] Szemplinska-Stupnicka W. The analytical predictive criteria for chaos and escape in nonlinear oscillators: A survey. Nonlin Dyn 1995;7:129–47.

[25] Melnikov VK. On the stability of the center for time periodic perturbations. Trans Mosc Math Soc 1963;12:1–57.

[26] Guckenheimer J, Holmes P. Nonlinear oscillations, dynamical systems and bifurcations of vectorfields. New York: Springer; 1983.

[27] Wiggins S. Introduction to applied nonlinear dynamical systems and chaos. New York: Spinger; 1990.

[28] Rega G, Lenci S. Identifying, evaluating, and controlling dynamical integrity measures in nonlinear mechanical oscillators. Nonlin. Anal. T. M. & A. 2005;63:902–14.

[29] Rega G, Lenci S. Dynamical integrity and control of nonlinear mechanical oscillators. J Vibr Control 2008;14:159–179.